reactions (Eqs. 3 to 5). Thus, although we may anticipate that the solvation dynamics measured involve substantial changes in the local solvation structure due to the solute size change, we expect that the energies associated with $(Na^+, e^-)^*$ formation are not chemically extreme and are representative of those associated with common solution-phase reactions.

This clear breakdown of LR implies that the solvent fluctuations coupled to the (Na^+, e^-) TCP are not Gaussian, and thus that the potential surfaces associated with these ET processes are highly nonparabolic. As a result, the Marcus theory of ET would poorly describe these ET processes. We anticipate that this could be an important consideration in many similar outer-sphere ET reactions, where substantial rearrangement of the local solvent structure could induce a similar LR breakdown. It is also important to note that the LR approximation is built on the idea that the same solvent-solute motions that underlie equilibrium fluctuations are also responsible for the nonequilibrium solvation dynamics (*3*). Although we observed a clear difference in the time dependence of two solvation pathways that reflects a breakdown of LR, observing an identical time dependence would not have guaranteed that the LR holds. This is because even when the specific molecular motions responsible for relaxing a nonequilibrium perturbation differ considerably from the solvent fluctuations active at equilibrium, LR may appear to be valid if the relevant nonequilibrium and equilibrium solvent motions happen to occur on similar time scales; what we have termed a hidden breakdown of LR (*29*, *30*). Overall, these findings demonstrate that an accurate assessment of solvation dynamics—and, by extension, our understanding of solution-phase chemical reactivity—must be considered directly at the molecular level in order to determine correctly how best to understand the solvent relaxation resulting from a given nonequilibrium perturbation.

References and Notes

1. R. A. Marcus, N. Sutin, *Biochim. Biophys. Acta* **811**, 265 (1985).
2. M. Maroncelli, *J. Mol. Liq.* **57**, 1 (1993).
3. D. Chandler, *Introduction to Modern Statistical Mechanics* (Oxford Univ. Press, New York, 1987).
4. R. M. Stratt, M. Maroncelli, *J. Phys. Chem.* **100**, 12981 (1996).
5. P. L. Geissler, D. Chandler, *J. Chem. Phys.* **113**, 9759 (2000).
6. D. Aherne, V. Tran, B. J. Schwartz, *J. Phys. Chem. B* **104**, 5382 (2000).
7. G. Tao, R. M. Stratt, *J. Chem. Phys.* **125**, 114501 (2006).
8. B. B. Laird, W. H. Thompson, *J. Chem. Phys.* **126**, 211104 (2007).
9. T. Fonseca, B. M. Ladanyi, *J. Phys. Chem.* **95**, 2116 (1991).
10. D. F. Underwood, D. A. Blank, *J. Phys. Chem. A* **109**, 3295 (2005).
11. D. S. Larsen, K. Ohta, Q. H. Xu, M. Cyrier, G. R. Fleming, *J. Chem. Phys.* **114**, 8008 (2001).
12. M. J. Bedard-Hearn, R. E. Larsen, B. J. Schwartz, *J. Chem. Phys.* **122**, 134506 (2005).
13. D. T. Bowron, J. L. Finney, A. K. Soper, *J. Am. Chem. Soc.* **128**, 5119 (2006).
14. M. J. Bedard-Hearn, R. E. Larsen, B. J. Schwartz, *J. Chem. Phys.* **125**, 194509 (2006).
15. I. B. Martini, E. R. Barthel, B. J. Schwartz, *Science* **293**, 462 (2001).
16. M. C. Cavanagh, R. E. Larsen, B. J. Schwartz, *J. Phys. Chem. A* **111**, 5144 (2007).
17. R. Catterall, J. Slater, M. C. R. Symons, *J. Chem. Phys.* **52**, 1003 (1970).
18. B. Bockrath, L. M. Dorfman, *J. Phys. Chem.* **77**, 1002 (1973).
19. F.-Y. Jou, G. R. Freeman, *Can. J. Chem.* **57**, 591 (1979).
20. A. E. Bragg, B. J. Schwartz, *J. Phys. Chem. B* **112**, 483 (2008).
21. A. E. Bragg, B. J. Schwartz, *J. Phys. Chem. A* **112**, 3530 (2008).
22. Methods are detailed in supporting material available on *Science* Online.
23. M. T. Lok, J. L. Dye, F. J. Tehan, *J. Phys. Chem.* **76**, 2975 (1972).
24. E. R. Barthel, B. J. Schwartz, *Chem. Phys. Lett.* **375**, 435 (2003).
25. O. Shoshana, J. L. Pérez Lustres, N. P. Ernsting, S. Ruhman, *Phys. Chem. Chem. Phys.* **8**, 2599 (2006).
26. V. Nagarajan, A. M. Brearley, T.-J. Kang, P. F. Barbara, *J. Chem. Phys.* **86**, 3183 (1987).
27. L. Reynolds, J. A. Gardecki, S. J. V. Frankland, M. L. Horng, M. Maroncelli, *J. Phys. Chem.* **100**, 10337 (1996).
28. A. C. Moskun, A. E. Jailaubekov, S. E. Bradforth, G. Tao, R. M. Stratt, *Science* **311**, 1907 (2006).
29. M. J. Bedard-Hearn, R. E. Larsen, B. J. Schwartz, *J. Phys. Chem. A* **107**, 4773 (2003).
30. M. J. Bedard-Hearn, R. E. Larsen, B. J. Schwartz, *Phys. Rev. Lett.* **97**, 130403 (2006).

31. This research was funded by NSF under grant number CHE-0603766. The authors thank R. E. Larsen for useful discussions and a critical reading of the manuscript.

Supporting Online Material

www.sciencemag.org/cgi/content/full/321/5897/1817/DC1
SOM Text
Figs. S1 to S4
References

9 June 2008; accepted 18 August 2008
10.1126/science.1161511

Mars' Paleomagnetic Field as the Result of a Single-Hemisphere Dynamo

Sabine Stanley,[1]* Linda Elkins-Tanton,[2] Maria T. Zuber,[2] E. Marc Parmentier[3]

Mars' crustal magnetic field was most likely generated by dynamo action in the planet's early history. Unexplained characteristics of the field include its strength, concentration in the southern hemisphere, and lack of correlation with any surface features except for the hemispheric crustal dichotomy. We used numerical dynamo modeling to demonstrate that the mechanisms proposed to explain crustal dichotomy formation can result in a single-hemisphere dynamo. This dynamo produces strong magnetic fields in only the southern hemisphere. This magnetic field morphology can explain why Mars' crustal magnetic field intensities are substantially stronger in the southern hemisphere without relying on any postdynamo mechanisms.

The Mars Global Surveyor mission showed that Mars possesses remanent crustal magnetic fields from a dynamo that was operational for a short time in Mars' early history (*1*). Remanent crustal magnetism is observed in early Noachian (>3.9 billion years old) crust in both the northern and southern hemispheres, except for much of the Tharsis volcanic province and the large impact basins Hellas and Argyre in the southern hemisphere, and Isidis and Utopia in the northern hemisphere. There is a conspicuous difference in the magnetic field intensities in the two hemispheres: The northern hemisphere contains only weak magnetic fields, whereas the southern hemisphere contains both strong and weak fields (*2*).

The timing of the dynamo is constrained by the observations that the floors of the large impact basins formed during the Late Heavy Bombardment [~3.9 billion years ago (Ga)] are not magnetized (*1*) and that the ancient Martian meteorite ALH84001 contains a remanent magnetic field dated earlier than 3.9 Ga (*3*). Most likely, the dynamo was active sometime between core formation (~4.5 Ga) and the Late Heavy Bombardment. The driving force for the dynamo, the intensity and morphology of the generated field, and the cause of the dynamo's demise are not well understood.

Another ancient Martian crustal feature is the hemispheric dichotomy. The northern and southern hemispheres have similar-aged crusts (*4*) but different topographies, thicknesses, and sediment covers (*5*). The northern hemisphere crust is low, thin, and covered with volcanic flows and sediments, whereas the southern hemisphere crust is high, thick, and largely devoid of sedimentary or volcanic resurfacing. Cratering evidence and the dichotomy's long wavelength suggest that the dichotomy is an ancient feature, directly related to crustal formation sometime between 4.5 and 3.9 Ga (*6*, *7*).

Because the crustal magnetic field and the dichotomy are similar in age, it is possible that their formation processes are related. Several endogenic mechanisms could explain both dichotomy formation and a concurrent dynamo sometime between 4.5 and 3.9 Ga. A hemispheric-scale (degree-1) pattern of mantle circulation resulting from either mantle convection in the presence of

[1]Department of Physics, University of Toronto, Toronto, ON M5S1A7, Canada. [2]Department of Earth, Atmospheric, and Planetary Sciences, Massachusetts Institute of Technology, Cambridge, MA 02139, USA. [3]Department of Geological Sciences, Brown University, Providence, RI 02912, USA.

*To whom correspondence should be addressed. E-mail: stanley@physics.utoronto.ca

radial viscosity variations (*8*, *9*), early magma ocean crystallization resulting in overturn (*10*, *11*), or superplumes resulting from destabilization of the mantle lower thermal boundary layer (*12*) provides degree-1 crustal structure along with sufficiently vigorous core convection to sustain a short-lived dynamo. Effects from a very large impact (*13*) or several large impacts (*14*) were also suggested early on but encountered difficulties (*15*, *16*). The probability of several large impacts forming the northern lowlands is low, and there is no evidence of individual basins. A single very large impact is statistically possible. Presently, the dichotomy boundary is not circular or elliptical; however, a recent analysis of crustal thickness (*17*) demonstrated that its original shape was elliptical. Therefore, the dichotomy boundary and northern lowlands could be the result of a giant low-angle impact.

Although explanations for dichotomy formation with concurrent magnetic field generation appear feasible, a serious problem is the markedly different intensities of the crustal magnetic fields in the northern and southern hemispheres. If the dynamo produced an axial-dipole-dominated magnetic field, similar to the geomagnetic field, and the northern and southern crusts formed at similar times with similar magnetic mineral densities and magnetic layer thicknesses, then one would expect crustal fields of similar strength in both hemispheres. Efforts to explain the hemispheric magnetic intensity differences generally involve postdynamo mechanisms in the northern hemisphere, such as hydrothermal alteration (*6*) or demagnetization resulting from early large impacts (*15*).

Here, we show that dynamo generation can also explain the hemispheric magnetic intensity differences, thereby removing the requirement for a postdynamo solution. All endogenic mechanisms involve hemispheric-scale mantle circulation, which will necessarily produce a degree-1 temperature anomaly in the mantle and hence at the core-mantle boundary (CMB). Numerical models have demonstrated that an exogenic (giant impact) mechanism could also produce a degree-1 temperature anomaly in the mantle and at the CMB (*18*). Because the CMB is the outer-bounding surface of the dynamo region, this temperature anomaly will result in a hemispheric heat flux variation on the outer boundary of the core. We therefore imposed a degree-1 variable heat flux pattern at the CMB in a dynamo simulation.

We used the numerical dynamo model of Kuang and Bloxham (*19*–*21*) with the parameter values given in Table 1. We imposed a heat flux across the CMB that was lower in the northern hemisphere than in the southern hemisphere (fig. S1). The heat flux variation on the CMB is relatively large, with the root mean square of the lateral variations three times the average superadiabatic heat flux. This may be reasonable for Mars when considering the relative temperatures of downwellings and upwellings at the CMB (*11*).

This spatially variable heat flux boundary condition produces a stable one-hemisphere dynamo. The radial component of the magnetic field is strongest and concentrated in the southern hemisphere with only weak fields in the northern hemisphere (Fig. 1A). Oscillatory hemispheric dynamos have been found in certain parameter regimes (*22*), producing a strong field in each hemisphere periodically. The dynamo in our simulation is different in that fields are actively gen-

Table 1. Nondimensional parameter values in the dynamo model. Model values are given for the Prandtl number ($Pr = \upsilon/\kappa$, where υ is the kinematic viscosity and κ is the thermal diffusivity); a magnetic Prandtl number ($q_\kappa = \kappa/\eta$ where η is the magnetic diffusivity); the Ekman number [$E = \upsilon/(2\Omega r_o^2)$, where Ω is the angular rotation rate of the planet and r_o is the core radius]; and the modified Rayleigh number [$Ra = \alpha g_o h_T r_o^2/(2\Omega\eta)$, where α, g_o, and h_T are the thermal expansion coefficient, the gravitational acceleration at the CMB, and the prescribed superadiabatic temperature gradient at the inner core boundary, respectively]. Using representative Mars values of $\alpha = 10^{-5}$ K^{-1}, $g_o = 3.5$ m s^{-2}, $r_o = 1700$ km, $\Omega = 7.1 \times 10^{-5}$ s^{-1}, and $\eta = 2$ m s^{-2}, combined with the chosen value for the Rayleigh number, implies a superadiabatic temperature gradient at the inner core boundary of 5×10^{-8} K m^{-1}, corresponding to a superadiabatic temperature gradient at the CMB of $h_T r_{io}^2 = 6 \times 10^{-9}$ K m^{-1} (where r_{io} is the inner to outer core radius ratio).

Parameter	Value
Pr	1
q_κ	1
E	2×10^{-5}
Ra	18,000

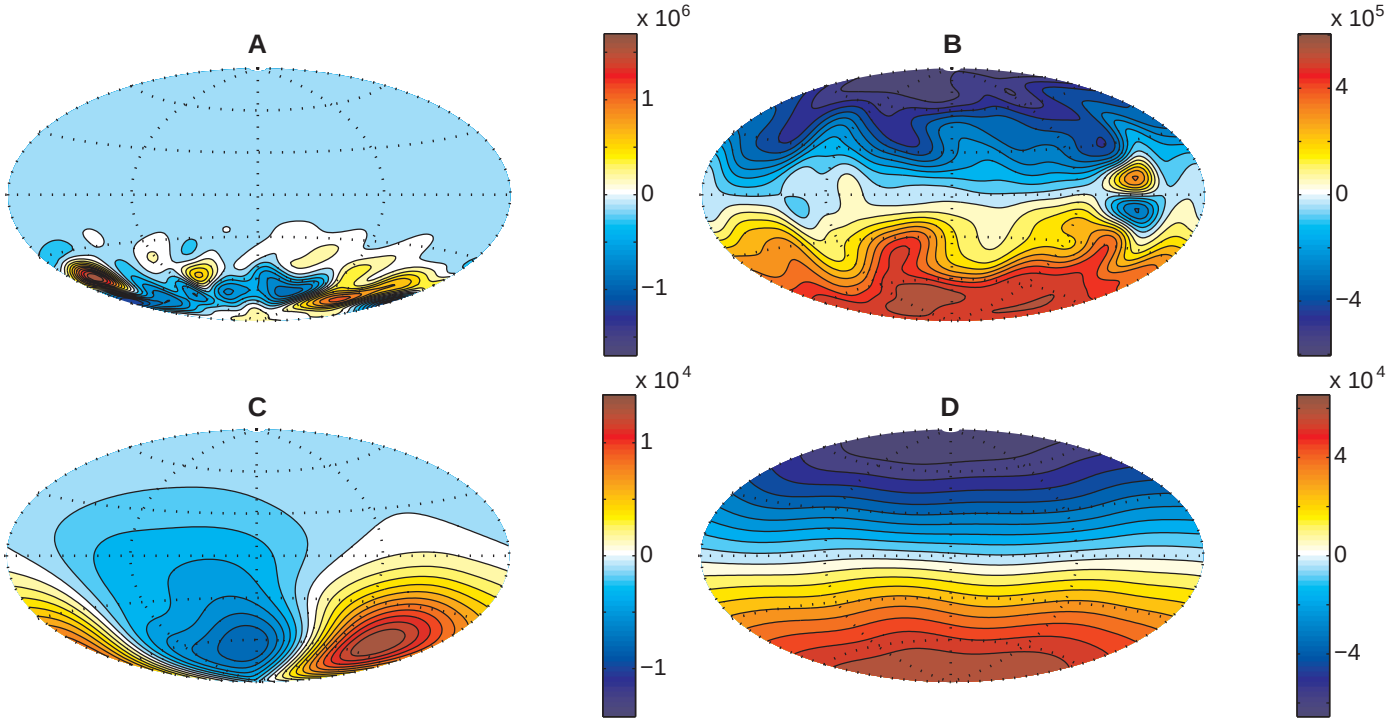

Fig. 1. Filled contours of the radial component of the magnetic field. For a model with a degree-1 heat flux outer-boundary condition, the field is plotted at the CMB in (**A**) and at the surface in (**C**). For a homogeneous heat flux outer-boundary condition, the field is plotted at the CMB in (**B**) and at the surface in (**D**). The CMB radius is 1700 km, the surface radius is 3400 km, and the units are nT.

erated in only a single hemisphere. The fields are smaller-scale and, although highly time-variable in morphology, remain strong in only the southern hemisphere (fig. S2). A dynamo model with a similar variable heat flux boundary condition as our model but with a different choice of velocity boundary condition does not produce a single-hemisphere dynamo (*23*), most likely because of the different force balances in the models [supporting online material (SOM) text].

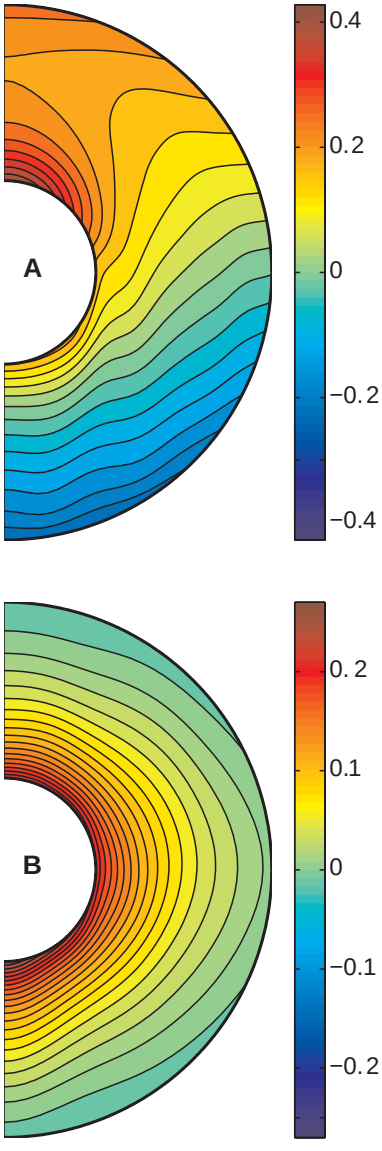

Fig. 2. Filled contours of the axisymmetric part of the nondimensional superadiabatic temperature. The profile for a model with a degree-1 heat flux outer-boundary condition is shown in (**A**) and for a model with a homogeneous heat flux outer-boundary condition in (**B**). The temperature plotted is with respect to the average CMB temperature, so positive values are hotter than the average CMB temperature and negative values are colder than the average CMB temperature. To dimensionalize in Kelvin, nondimensional values should be multiplied by 0.085.

The radial field at the CMB in our model was more intense than that in a model with the same parameter values but with a homogeneous heat flux boundary condition that produced an axial-dipolar dynamo (Fig. 1B). However, because the power in the field components fell off faster with distance for smaller scales, the magnetic field at the surface was slightly weaker in our variable heat flux model than in the homogeneous heat flux model but was the same order of magnitude (Fig. 1, C and D).

The hemispheric boundary condition in the model changed the equatorial symmetry of the superadiabatic temperature (Fig. 2), affecting the dominant force balance in the core. This had a substantial effect on the velocity fields of the core in our model (Fig. 3A). The zonal flows, mainly resulting from thermal winds, were equatorially antisymmetric and therefore did not adhere to the Taylor-Proudman constraint, which is expected to hold when Coriolis and pressure forces dominate in the core (*24*). In addition, the meridional circulation pattern was concentrated in the southern hemisphere rather than filling the whole core, as in a model with homogeneous heat flux boundary conditions (Fig. 3B). The convection rolls were concentrated in the hemisphere with the colder CMB temperature and generated the strongest dynamo action in this region.

Our results suggest that the concentration of strong crustal fields in the southern hemisphere of Mars could result from a dynamo that produced a magnetic field concentrated in the southern hemisphere. In this scenario, no postdynamo process is required to remove a strong crustal field in the northern hemisphere. Although large basins are demagnetized in the northern hemisphere (as they are in the southern hemisphere), this mechanism can explain why none of the magnetized regions

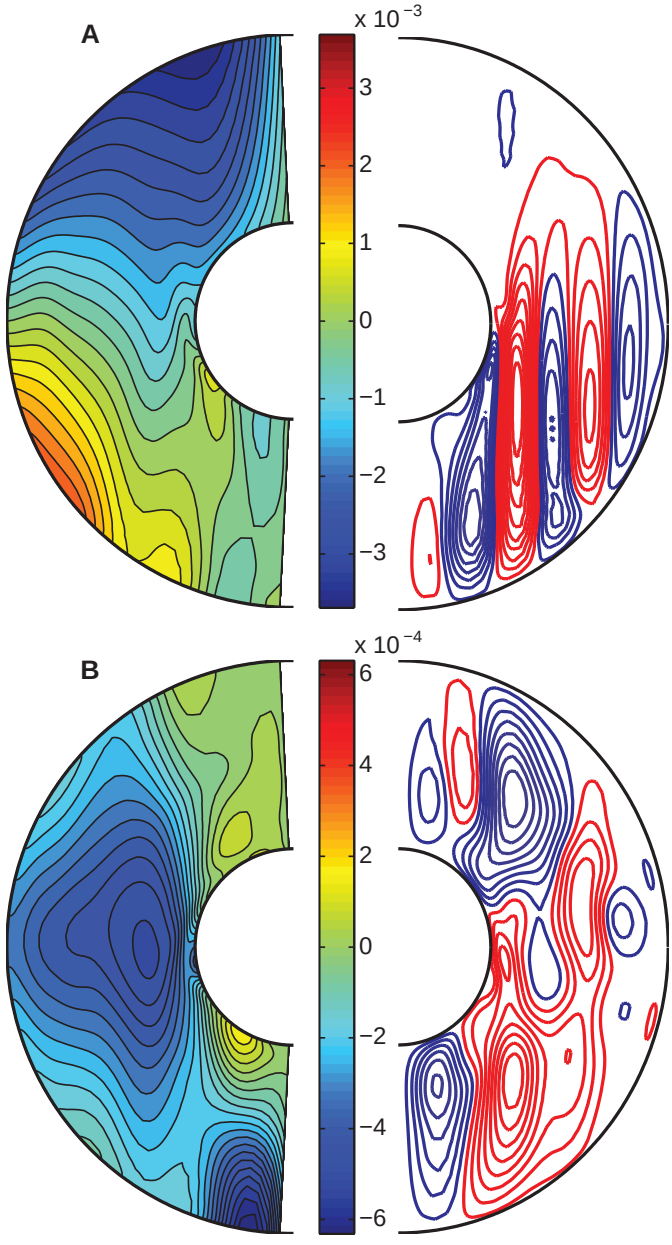

Fig. 3. Axisymmetric component of the nondimensional velocity field. Filled contours of the zonal velocity are shown on the left, and stream lines of the meridional circulation are shown on the right for a model with a degree-1 heat flux outer-boundary condition (**A**) and a model with a homogeneous heat flux outer-boundary condition (**B**). For the zonal velocity, red indicates prograde zonal flow, and blue, retrograde zonal flow. For the meridional circulation, red indicates prograde circulation, and blue, retrograde circulation. The color bars apply to the zonal velocity figures only, and the units are m s^{-1}. The intensity of the meridional circulation is prescribed by the spacing of the stream lines.

in the northern hemisphere are as strong as the regions in the south.

In addition to explaining the occurrence of a strong field in only one hemisphere, our model is also able to explain the conflicts between various Mars paleomagnetic studies and rotational stability studies. The inferred paleomagnetic pole positions vary in location depending on the individual crustal anomaly used (*25*, *26*). Some of the paleopoles are also located in equatorial regions near the Tharsis bulge and hence are far from the current geographic poles. This has been interpreted as evidence for a large true polar wander event that relocated Tharsis from polar to equatorial regions in early Mars history (*27*). However, large Tharsis-driven true polar wander is in conflict with rotational stability studies (*28*, *29*) that demonstrate that the present-day gravitational figure of Mars favors a small Tharsis-driven true-polar wander scenario.

An assumption made in the paleomagnetic studies is that the dynamo-generated magnetic field was axial-dipolar dominated. This assumption implies that the magnetic pole coincided with the rotation pole and is used extensively in Earth paleomagnetic studies. Our models would dictate that the Mars dynamo-generated field was not axial-dipolar dominated and hence that the magnetic poles would not coincide with the rotation poles, rendering paleopole interpretations useless. In addition, because our dynamo-generated fields are multipolar, individual crustal magnetic fields at different locations can point to different paleomagnetic poles, thereby explaining the discrepancies in the different paleomagnetic studies.

A single-hemisphere dynamo also has implications for evolution of the martian atmosphere. A strong dynamo-generated magnetic field can more easily explain the intense crustal magnetism. However, efficient atmospheric erosion, necessary to explain the loss of Mars' early thick atmosphere, favors a weak internal magnetic field (*30*). Our single-hemisphere dynamo may provide an elegant solution to this problem because the northern hemisphere would be prone to atmospheric removal early in solar system history when the young Sun was more active (*31*), but the southern hemisphere could still possess a strong magnetic field in which the crustal rocks could magnetize.

References and Notes

1. M. H. Acuna *et al.*, *Science* **284**, 790 (1999).
2. B. Langlais, M. E. Purucker, M. Mandea, *J. Geophys. Res.* **109**, E02008 (2004).
3. B. P. Weiss *et al.*, *Earth Planet. Sci. Lett.* **201**, 449 (2002).
4. L. A. Edgar, H. V. Frey, *Geophys. Res. Lett.* **35**, L02201 (2008).
5. M. T. Zuber *et al.*, *Science* **287**, 1788 (2000).
6. S. C. Solomon *et al.*, *Science* **307**, 1214 (2005) and references therein.
7. H. V. Frey, *J. Geophys. Res.* **111**, E08S91 (2006).
8. S. Zhong, M. T. Zuber, *Earth Planet. Sci. Lett.* **189**, 75 (2001).
9. J. H. Roberts, S. Zhong, *J. Geophys. Res.* **111**, E06013 (2006).
10. L. T. Elkins-Tanton, E. M. Parmentier, P. C. Hess, *Meteorit. Planet. Sci.* **38**, 1753 (2003).
11. L. T. Elkins-Tanton, S. E. Zaranek, E. M. Parmentier, P. C. Hess, *Earth Planet. Sci. Lett.* **236**, 1 (2005).
12. Y. Ke, V. S. Solomatov, *J. Geophys. Res.* **111**, E10001 (2006).
13. D. E. Wilhelms, S. W. Squyres, *Nature* **309**, 138 (1984).
14. H. Frey, R. A. Shultz, *Geophys. Res. Lett.* **15**, 229 (1988).
15. F. Nimmo, M. S. Gilmore, *J. Geophys. Res.* **106**, 12315 (2001).
16. T. R. Watters, P. J. McGovern, R. P. Irwin III, *Annu. Rev. Earth Planet. Sci.* **35**, 621 (2007).
17. J. C. Andrews-Hanna, M. T. Zuber, W. B. Banerdt, *Nature* **453**, 1212 (2008).
18. W. A. Watters, M. T. Zuber, B. H. Hager, *J. Geophys. Res.*, in press.
19. W. Kuang, J. Bloxham, *Nature* **389**, 371 (1997).
20. W. Kuang, J. Bloxham, *J. Comput. Phys.* **153**, 51 (1999).
21. Additional information on the numerical methods is available as supporting material on *Science* Online.
22. E. Grote, F. H. Busse, *Phys. Rev. E* **62**, 4457 (2000).
23. G. A. Glatzmaier, R. S. Coe, L. Hongre, P. H. Roberts, *Nature* **401**, 885 (1999).
24. M. Kono, P. H. Roberts, *Rev. Geophys.* **40**, 1013 (2002).
25. Y. Quesnel, B. Langlais, C. Sotin, *Planet. Space Sci.* **55**, 258 (2007), and references therein.
26. B. Langlais, M. Purucker, *Planet. Space Sci.* **55**, 270 (2007); and references therein.
27. K. F. Sprenke, L. L. Baker, A. F. Williams, *Icarus* **174**, 486 (2005); and references therein.
28. A. Daradich *et al.*, *Icarus* **194**, 463 (2008).
29. J. T. Perron, J. X. Mitrovica, M. Manga, I. Matsuyama, M. A. Richards, *Nature* **447**, 840 (2007).
30. V. Dehant *et al.*, *Space Sci. Rev.* **129**, 279 (2007).
31. Y. N. Kulikov *et al.*, *Space Sci. Rev.* **129**, 207 (2007).

32. S.S. is partially funded by the National Science and Engineering Research Council (NSERC) of Canada. The numerical simulations in this study were performed on supercomputing resources partially funded by the Canadian Foundation for Innovation (CFI) and the Ontario Research Fund (ORF).

Supporting Online Material

www.sciencemag.org/cgi/content/full/321/5897/1822/DC1
Materials and Methods
SOM Text
Figs. S1 and S2

29 May 2008; accepted 19 August 2008
10.1126/science.1161119

The Structure and Dynamics of Mid-Ocean Ridge Hydrothermal Systems

D. Coumou,* T. Driesner, C. A. Heinrich

Sub-seafloor hydrothermal convection at mid-ocean ridges transfers 25% of the Earth's heat flux and can form massive sulfide ore deposits. Their three-dimensional (3D) structure and transient dynamics are uncertain. Using 3D numerical simulations, we demonstrated that convection cells self-organize into pipelike upflow zones surrounded by narrow zones of focused and relatively warm downflow. This configuration ensures optimal heat transfer and efficient metal leaching for ore-deposit formation. Simulated fluid-residence times are as short as 3 years. The concentric flow geometry results from nonlinearities in fluid properties, and this may influence the behavior of other fluid-flow systems in Earth's crust.

Hydrothermal convection at mid-ocean ridge spreading centers transports a major part of Earth's total heat flux, substantially affects the chemistry of crust and overlying ocean, and provides nutrients for chemosynthetic life on and beneath the sea floor. Mass, heat, and associated chemical fluxes from the crust to the ocean at mid-ocean ridge spreading centers are large (*1*, *2*). Fundamental features of this flow, such as the location of seawater recharge and the relative importance of off- versus along-axis convection, are still uncertain. Recent studies of active (*3*) and ancient (*4*) systems show that discharge can be highly focused in pipelike regions, possibly continuing to the base of the hydrothermal system (*3*). Recharge is often thought to occur over extensive areas (*5*, *6*), with off-axis faults guiding fluid pathways toward the base of the hydrothermal system. A common alternative view is that of fluid circulation being restricted to a high-permeability along-axis zone (*7*, *8*). Micro-earthquake data indicate that recharge can be focused close to the spreading center in some systems (*9*).

Recent two-dimensional (2D) numerical studies that included accurate thermodynamic properties of water have shown that the nonlinear dependence of fluid properties on pressure and temperature is a first-order control, determining the self-organization of convection cells (*10*–*12*). Quantitative 3D numerical models have been applied to low-permeability (*13*) or sedimented systems (*14*) and to a configuration with an along-axis high-permeability fracture (*15*, *16*) but not to the more highly permeable basaltic systems, which represent the greater and most active part of mid-ocean ridge spreading centers. Here, we describe a 3D model that represents the hydrothermal system without geological complexity so as to identify the first-order physical factors controlling the behavior of mid-ocean ridge convection cells.

The governing equations are an appropriate version of Darcy's law (*17*), conservation of mass and energy in an incompressible porous medium (*12*) and an accurate equation of state for pure water (*18*). Using pure water substantially reduces the computational complexity because pure water above the critical pressure (21.1 MPa) is always a single-phase fluid with properties closely resembling those of seawater. Two-dimensional across-axis simulations including the full-phase

Department of Earth Sciences, Eidgenössische Technische Hochschule–Zurich, Clausiusstrasse 25, Zurich 9082, Switzerland.

*To whom correspondence should be addressed. E-mail: coumou@pik-potsdam.de

Mars' Paleomagnetic Field as the Result of a Single-Hemisphere Dynamo

Sabine Stanley, Linda Elkins-Tanton, Maria T. Zuber and E. Marc Parmentier (September 26, 2008)

Science **321** (5897), 1822-1825. [doi: 10.1126/science.1161119]

Editor's Summary